



Effect of microstructure inhomogeneity on mechanical properties of different zones in TA15 electron beam welded joints

Cai-yan DENG¹, Ce LIU¹, Bao-ming GONG¹, Cheng-ze ZHANG², Chang LIU¹, Yong LIU¹

1. Key Laboratory of Advanced Joining Technology of Tianjin, School of Materials Science and Engineering, Tianjin University, Tianjin 300350, China;
2. Changguang Satellite Technology Co., Ltd., Changchun 130000, China

Received 6 June 2019; accepted 20 November 2019

Abstract: The effects of microstructure inhomogeneity on the mechanical properties of different zones in TA15 electron beam welded joints were investigated using a micromechanics-based finite element method. Considering the indentation size effect, the mechanical properties for constituent phases of the base metal (BM) and heat affected zone (HAZ) were determined by the instrumented nano-indentation test. The macroscopic mechanical properties of BM and HAZ obtained from the tensile test agree well with the numerical results. The incompatible deformation between the constituent phases tends to localize along the softer primary phase α where failure usually initiates in form of localized plastic strain. Compared with the BM, the mechanical properties of constituent phases in the HAZ differ substantially, leading to more serious strain localization behavior.

Key words: microstructure inhomogeneity; strain localization; electron beam welding; titanium alloy; finite element analysis

1 Introduction

As a kind of key structural material, titanium alloys are widely used in aviation and aerospace industries due to their excellent mechanical and physical properties [1–3]. Electron beam welding (EBW) is a promising method to join the titanium alloy because of high energy density, relatively low heat input and small distortion [4–8]. However, welding is a non-equilibrium process of rapid heating and solidification, which makes the microstructure of the welded joints inhomogeneous [9]. It is of great importance to study the microstructure inhomogeneity of different zones in welded joints from the microscopic perspective, whereas the topic has still not been well understood up to the present date.

It is well known that the microstructure of the

base metal (BM) mainly consists of the primary phase α (α_p) as well as transformed β matrix (β_t) as the case in all Ti–Al alloys [10,11], and the heat affected zone (HAZ) is mainly made up of α_p and acicular martensitic phase α' (α') in the TA15 titanium alloy welded joints [12]. To evaluate the effects of microstructure inhomogeneity on the macroscopic mechanical properties of multi-phase materials, several experimental techniques and numerical simulation methods have been integrated to predict evolution of deformation behavior and failure modes of multi-phase materials from their microstructures [13–17]. LEE et al [18] investigated the relationship between the residual indentation profiles and the strain hardening exponents of the indented materials by a reverse analysis, which minimized the sensitivity of the data and experimental errors and improved the accuracy in the nano-indentation. SHI et al [19]

studied the elastic–plastic deformation process of different constituent phases in TC6 titanium alloy during the tensile process using micromechanics-based finite element simulation, revealing that the inhomogeneity of the microstructure could cause the uncoordinated deformation of the multi-phase alloy. MOEINI et al [20] used a two-dimensional representative volume element (RVE) to calculate the mechanical properties of different zones in the welded joints by finite element method. The results accurately predicted the weak area of the joints. JI et al [21] adopted a micromechanics-based finite element model to investigate the effect of phase content and phase properties on strain localization of two-phase titanium alloy and predicted the macroscopic stress–strain responses. From the analysis above, micromechanics-based finite element methods are appropriate for predicting the macroscopic mechanical response and microstructural deformation of the multi-phase materials.

In this work, microstructure inhomogeneity of different zones in TA15 titanium alloy welded joints was studied using the finite element analysis. The tensile test was performed to validate the numerical prediction, and the strain localization behavior between BM and HAZ was compared by the simulated results.

2 Experimental

2.1 Welding process

The experimental material in the current study is a TA15 titanium alloy, and the chemical composition is given in Table 1. The butt joints were prepared by the electron beam welding process. Welding parameters such as accelerating voltage, focusing current, welding speed, electron beam current, and heat input were 140 kV, 340 mA, 400 mm/min, 36 mA, and 460 J/mm, respectively.

Table 1 Chemical composition of TA15 titanium alloy (wt.%)

Al	Mo	Zr	V	Fe	O	C	N	Ti
6.83	1.51	1.97	1.60	0.11	0.074	0.008	0.003	Bal.

2.2 Instrumented nano-indentation test

The nano-indentation specimens were cut from the BM and HAZ of the welded joints followed by grinding with SiC sandpaper and the electrolytic

polishing, and corroded by hydrofluoric acid solution, respectively. The test was performed by a nano indenter G200 equipped with a Berkovich indenter. The indentation tester was calibrated initially by a fused silica standard specimen. The test was carried out in the maximum load control mode, where the load was increased from 40 to 100 mN progressively.

2.3 Tensile test and microstructural observations

The dimensions of the miniature tensile specimen are shown in Fig. 1, and the thickness of the sample is 0.8 mm. The specimens were fabricated by electric discharge machining (EDM) from the BM and HAZ of the welded joints. The microstructure was observed by the SEM, as shown in Fig. 2. The average volume fractions of α_p

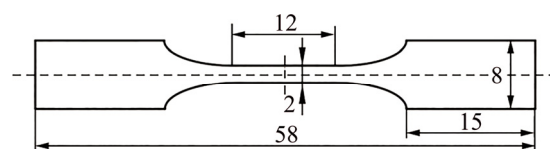


Fig. 1 Dimensions of miniature tensile specimen (unit: mm)

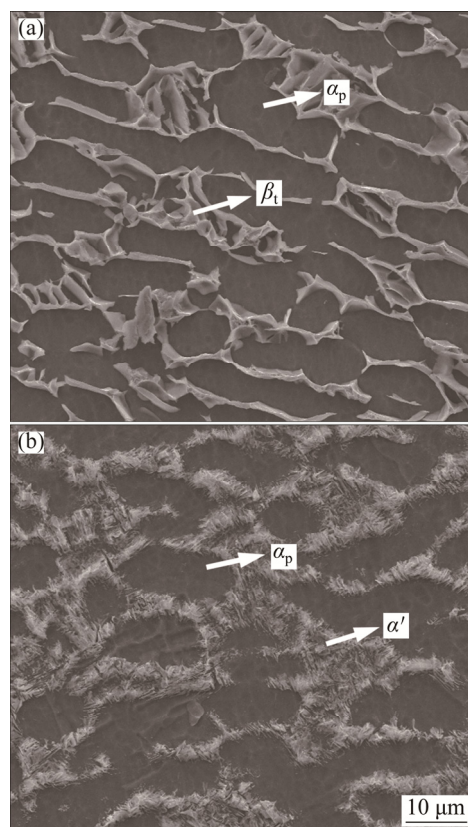


Fig. 2 SEM images of TA15 titanium alloy welded joints: (a) BM; (b) HAZ

phase and β_t phase in the BM were determined by the SEM micrographs from 5 locations in the specimen, and the average volume fraction of α_p phase was 63.67% measured by ImageJ software. Similarly, the average volume fraction of α_p phase in the HAZ was 51.99%. The tensile tests were carried out by an Instron 5848 instrument at room temperature with a loading rate of 0.05 mm/min.

3 Micromechanics-based finite element modeling

3.1 Mechanical properties of phases obtained by instrumented nano-indentation test

Considering indentation size effect (ISE) [16], a calculation method proposed by ZHANG et al [22,23] was used to determine the mechanical properties of each phase. It is assumed that the elastic–plastic behavior of the tested phase satisfies the following description [15]:

$$\begin{cases} \sigma = E\varepsilon, & \sigma \leq \sigma_y \\ \sigma = \sigma_y \left(1 + \frac{E}{\sigma_y} \varepsilon_p \right)^n, & \sigma > \sigma_y \end{cases} \quad (1)$$

where E is the elastic modulus, σ_y is the yield strength, n is the work hardening exponent, and ε_p is the nonlinear part of the total strain ε , which defines as

$$\varepsilon_p = \varepsilon - \varepsilon_y \quad (2)$$

where ε_y is the yield strain.

Figures 3(a) and (b) show the load–depth curves of α_p phase and β_t phase of the BM in the TA15 titanium alloy welded joints. The indentation in both phases is accurately pressed into the target region. It is generally believed that the size of the plastic zone formed around the indentation is approximately twice that of the impression [20]. The indentation tests avoid the influence of the

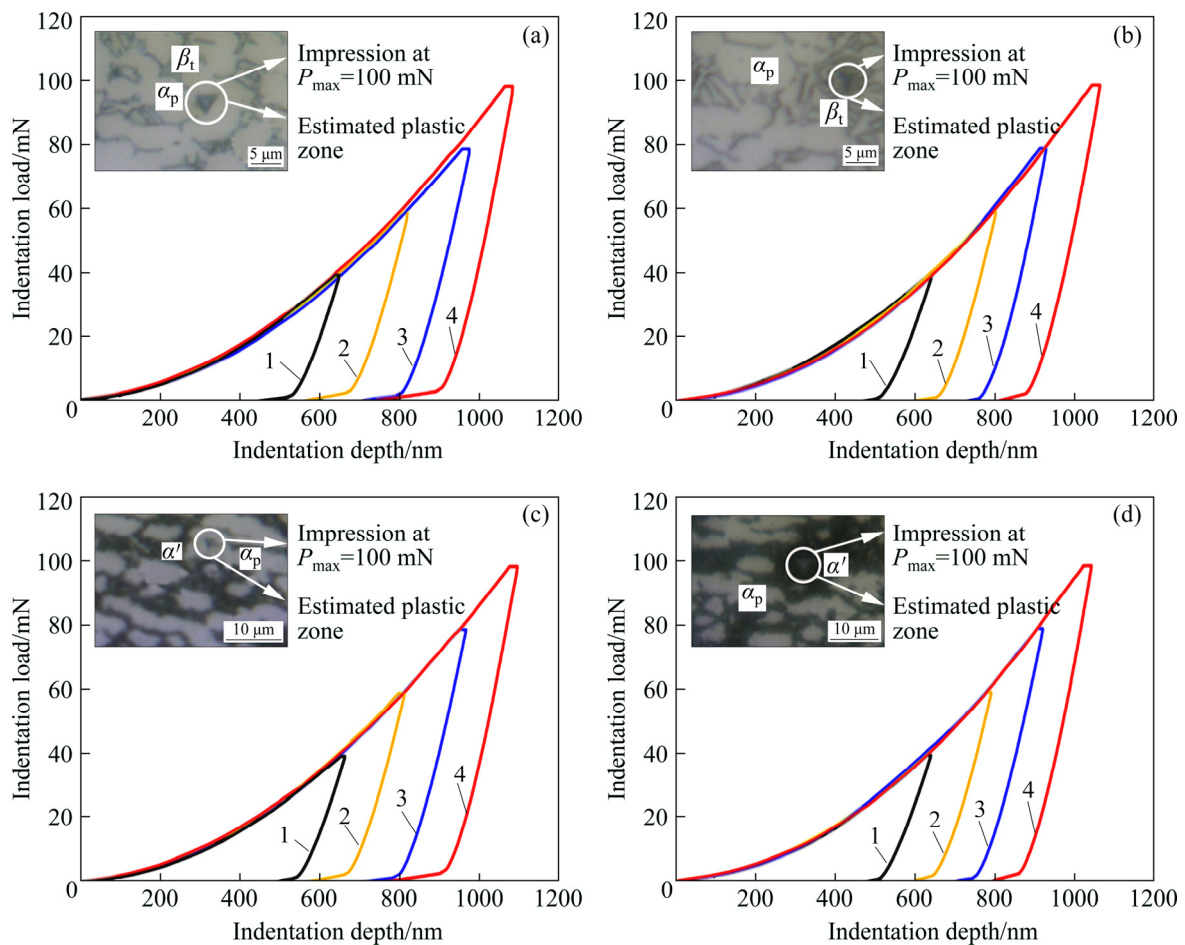


Fig. 3 Indentation load–depth curves recorded during nano-indentation tests with insets showing representative indentation impressions: (a) α_p in BM; (b) β_t in BM; (c) α_p in HAZ; (d) α' in HAZ (1—Applied maximum load of 40 mN; 2—Applied maximum load of 60 mN; 3—Applied maximum load of 80 mN; 4—Applied maximum load of 100 mN)

neighboring phase, which precisely reflects the mechanical properties of both phases in the BM. Similarly, the load–depth curves of the α_p phase and the α' phase in the HAZ are shown in Figs. 3(c) and (d).

The elastic modulus E of each phase is obtained directly from the test data, the yield strength σ_y is determined according to the following calculation method [24]:

$$\frac{H}{H_0} = \sqrt{1 + \frac{h^*}{h}} \quad (3)$$

where H is the nominal hardness under a given indentation depth h , h^* is a characteristic length depending on the shape of indenter and the material, and H_0 is the size independent of plastic hardness. The function is established by fitting the linear relation of the nominal hardness value H^2 and the reciprocal of the indentation $1/h$. Therefore, the value of H_0 can be estimated when $1/h$ approaches zero [25].

The yield strength is calculated according to the following formulas [23]:

$$H_0 = 4.15\sigma_y \quad (4)$$

A specific stress $\sigma_{0.033}$ at $\varepsilon_p=0.033$ can be calculated from the following equation [15]:

$$\frac{C}{\sigma_{0.033}} = -1.131 \left[\ln \left(\frac{E_r}{\sigma_{0.033}} \right) \right]^3 + 13.635 \left[\ln \left(\frac{E_r}{\sigma_{0.033}} \right) \right]^2 - 30.594 \left[\ln \left(\frac{E_r}{\sigma_{0.033}} \right) \right] + 29.467 \quad (5)$$

where C is the loading curvature of the load–depth curve, and E_r is the reduced modulus, which is calculated using the following relation [26]:

$$\frac{1}{E_r} = \frac{1-\nu^2}{E} + \frac{1-\nu_i^2}{E_i} \quad (6)$$

where ν is Poisson ratio of specimen, $E_i=1140$ GPa and $\nu_i=0.07$ are the elastic modulus and Poisson ratio for diamond indenter. The Poisson ratio for different zones of the welded joints is 0.33. The specific stress $\sigma_{0.033}$ can be obtained according to Eq. (5). Therefore, work hardening exponent n for each phase can be calculated by the following equation:

$$\sigma_{0.033} = \sigma_y \left(1 + 0.033 \frac{E}{\sigma_y} \right)^n \quad (7)$$

Finally, the mechanical properties of α_p phase

and β_t phase in the BM, and those of α_p phase and α' phase in the HAZ are obtained, and the stress–strain curves are plotted in Fig. 4. In the BM, the microstructure consists of α_p phase and β_t phase: the elastic modulus E of α_p phase is higher than that of β_t phase; the yield strength σ_y and the work hardening exponent n of α_p phase are lower than those of β_t phase. Therefore, the mechanical properties of the microstructure are inhomogeneous. Similarly, the HAZ has an inhomogeneous microstructure. By the comparison, it is found that the more significant difference exists between the two phases of the HAZ.

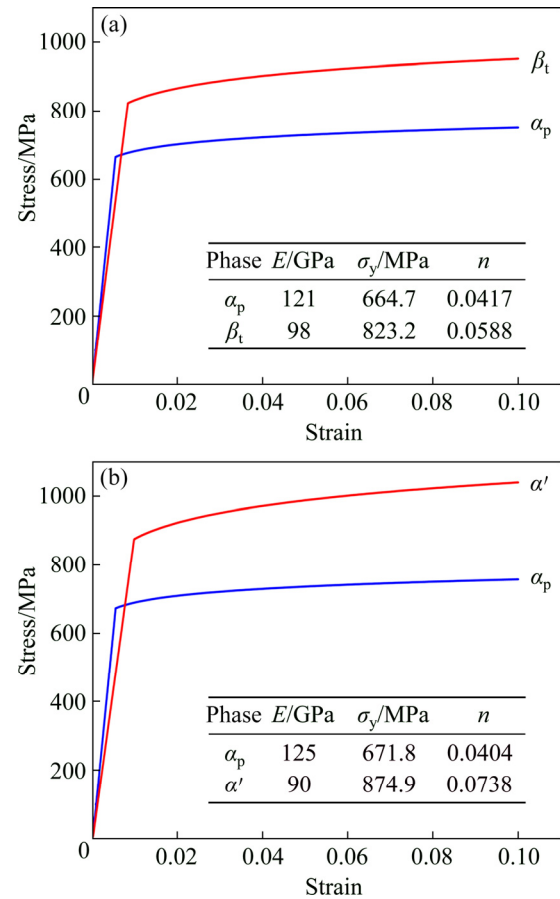


Fig. 4 Stress–strain curves of constituent phases: (a) BM; (b) HAZ

3.2 Finite element modeling

The commercial finite element code ABAQUS is used in the analyses. The micromechanics-based finite element models are established by representative volume elements (RVEs) which are generated from the SEM images (Fig. 2). The procedure includes geometry modeling, constitutive modeling, meshing, applying boundary condition, and finite element calculation, which is shown in

Fig. 5. The image processing software is used to distinguish two kinds of phases and convert them into a binary diagram according to the gray value. The finite element models are established by matching one pixel to one finite element. The finite element model (80 μm × 80 μm) contains 640000 4-node bilinear plane stress quadrilateral (CPS4) elements. Figure 6 shows finite element models for the RVEs. The volume fractions of α_p are 64.15% in the BM and 52.41% in the HAZ by image processing software, approximately equal to the experimental data (Fig. 2). The models accurately reflect the microstructure distribution of different zones in the welded joints [27].

In order to reflect the deformation behavior of the material in the tensile process, the periodic boundary condition (PBC) is applied to the RVE as follows:

$$u_i^p - u_i^q = \varepsilon_{ij}(x_j^q - x_j^p) \tag{8}$$

where *u* represents the translation displacement of counterpart nodes, *i*, *j*(=1, 2) are the degrees of

freedom in the two-dimension problem, *p* and *q* refer to the nodes on opposite sides of the unit cell, ε_{ij} is the average macroscopic strain, and *x* is the coordinate of the node. It is assumed that the mechanical properties of the material are isotropic, which are obtained by the instrumented indentation test in the previous sections. Finally, the calculation process is performed by finite element software.

4 Results and discussion

4.1 Verification of simulated results

The mechanical properties of each phase obtained from nano-indentation experiments were imported into the finite element model for calculation. Five regions randomly selected from the BM and HAZ were applied to the model. The parameters and boundary conditions of these models were identical. With the established micromechanics-based finite element models, the predicted mechanical responses of the RVEs during the tensile process are shown in Fig. 7. It is found

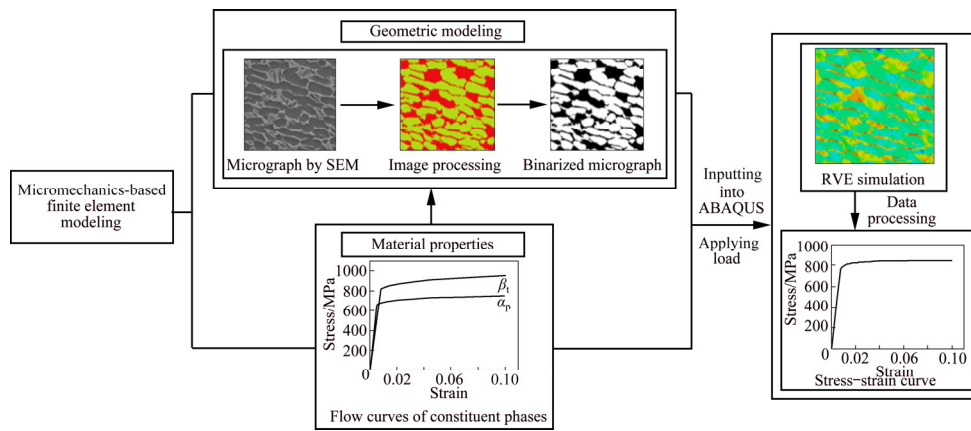


Fig. 5 Procedure of micromechanics-based finite element modeling

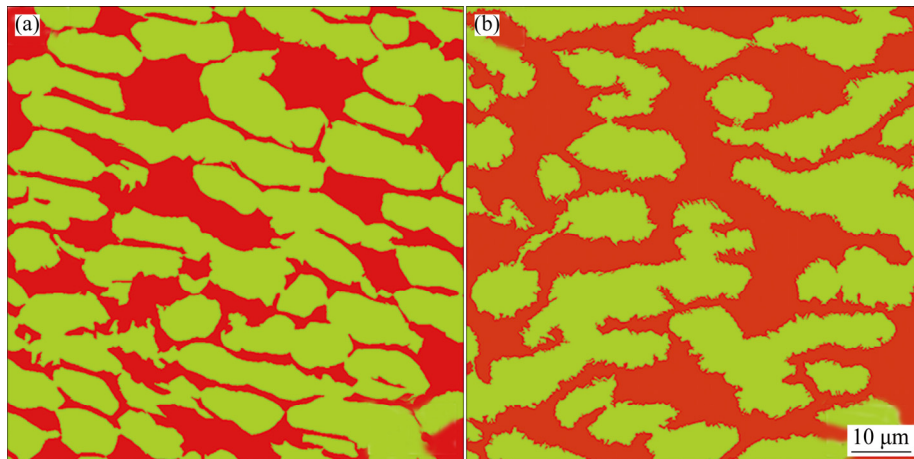


Fig. 6 Finite element models for RVEs: (a) BM; (b) HAZ

that there are no noticeable variations among the simulated stress–strain curves. Therefore, the selected RVE used in the simulation is an eligible model. Figure 8 shows the comparison of the stress–strain curves between the simulation and the tensile test, reaching a good agreement. Accordingly, the simulated results can reflect the stress–strain behavior in the actual tensile process.

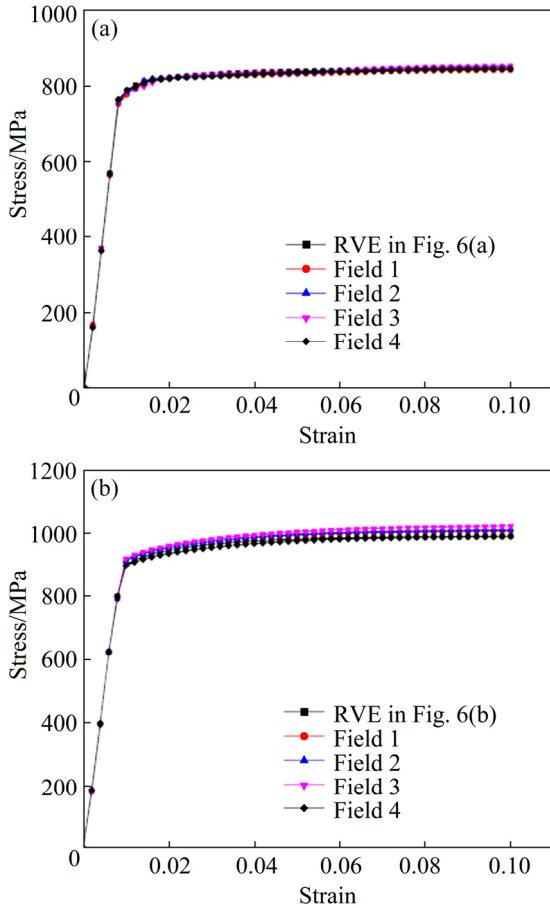


Fig. 7 Simulated stress–strain curves for five random fields: (a) BM; (b) HAZ

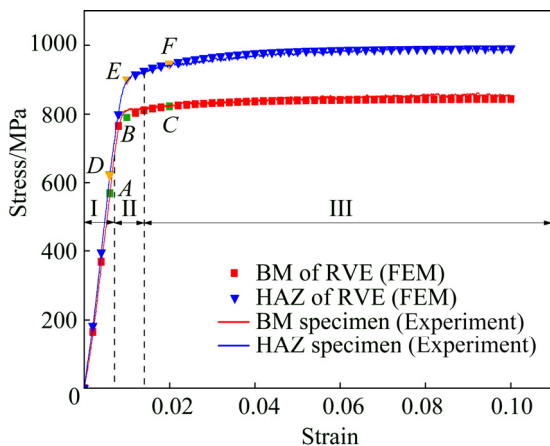


Fig. 8 Comparison between experimental stress–strain curves and simulated results

4.2 Inhomogeneous stress–strain distribution

The mechanical response of the multi-phase materials is governed by the microscopic stress and strain partitioning behavior among the constituent phases. The whole deformation process can be divided into three stages from Fig. 8: (I) the elastic deformation stage; (II) the elastic–plastic deformation stage; (III) the plastic deformation stage. It is supposed that the difference of constituent phase of the BM or HAZ in elastic–plastic properties gives rise to inhomogeneous strain distributions, and the strain localization at larger deformation may dominate the plastic deformation until crack initiation and total failure [22]. Six points (*A*, *B*, *C* in the BM, and *D*, *E*, *F* in the HAZ) are selected to show the distributions of equivalent plastic strain (PEEQ) and von Mises stress at different macroscopic strain levels (ε_m) of the BM and HAZ in Figs. 9 and 10, respectively. In stage I, the deformation in the two phases is relatively uniform in the BM. Besides, at this stage, the β_t phase tends to dominate the stress partition, as shown in Figs. 9(a) and (d). However, there are larger strain and stress localization zones and higher stress and strain values in the HAZ (Figs. 10(a) and (d)), which may be due to the larger difference of elastic modulus between the constituent phases in the HAZ. As the macroscopic strain increases, stage II starts when the specific stress of the α_p phase reaches yield stress. Then, the α_p phase occurs plastic deformation in this stage; however, the harder β_t phase undergoes only elastic deformation due to higher yield strength, as shown in Figs. 9(b) and (e). Therefore, the yielding initiation of BM is controlled by the α_p phase [28]. On the other hand, due to larger difference of yield strength between the constituent phases, the HAZ has larger deformation incompatibility (Fig. 10(b)). In the last stage, the β_t phase reaches yield stress as well and starts to deform plastically. Due to the fact that the flow stress of the β_t phase is higher than that of the α_p phase (Fig. 4), the α_p phase bears the higher strain, and the β_t phase undergoes the higher stress, as shown in Figs. 9(c) and (f), respectively. Besides, because of the constraint by the adjacent α_p phase, the plastic strain tends to spread into the β_t phase and leads to higher stress along the interface between α_p phase and β_t phase. Compared with the BM, the areas of strain localization in the softer

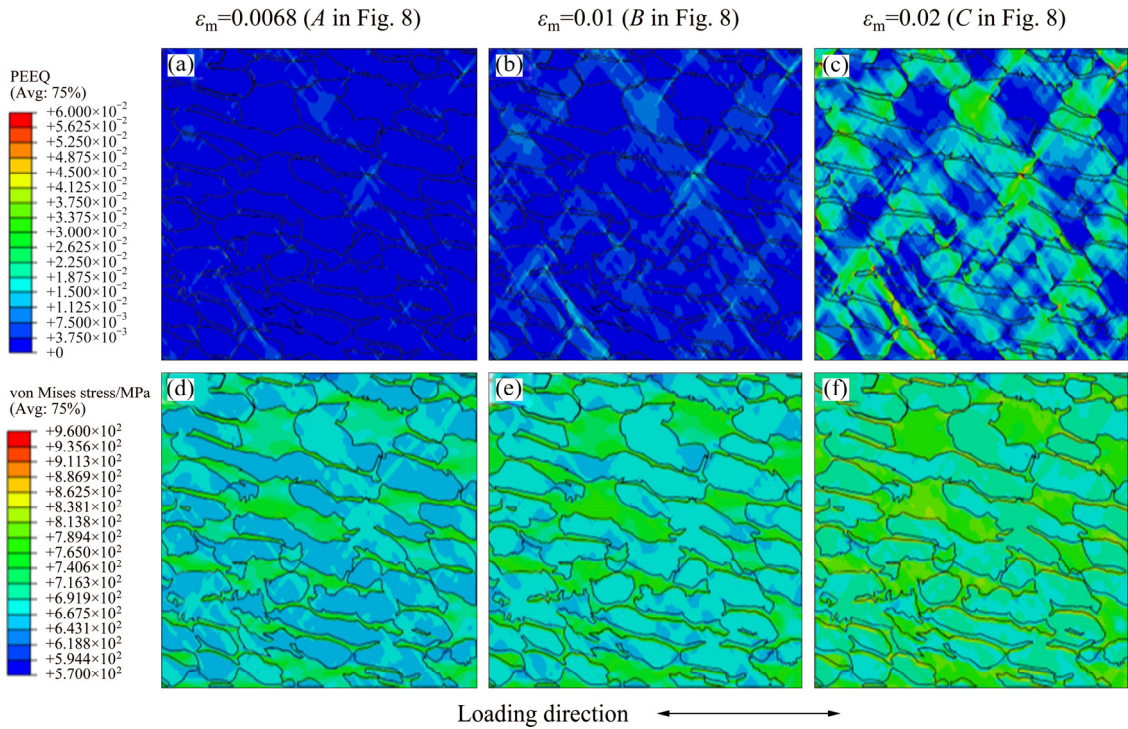


Fig. 9 Distributions of equivalent plastic strain (PEEQ) and von Mises stress at different macroscopic strains (ϵ_m) in BM (Grain boundaries are traced by black pen)

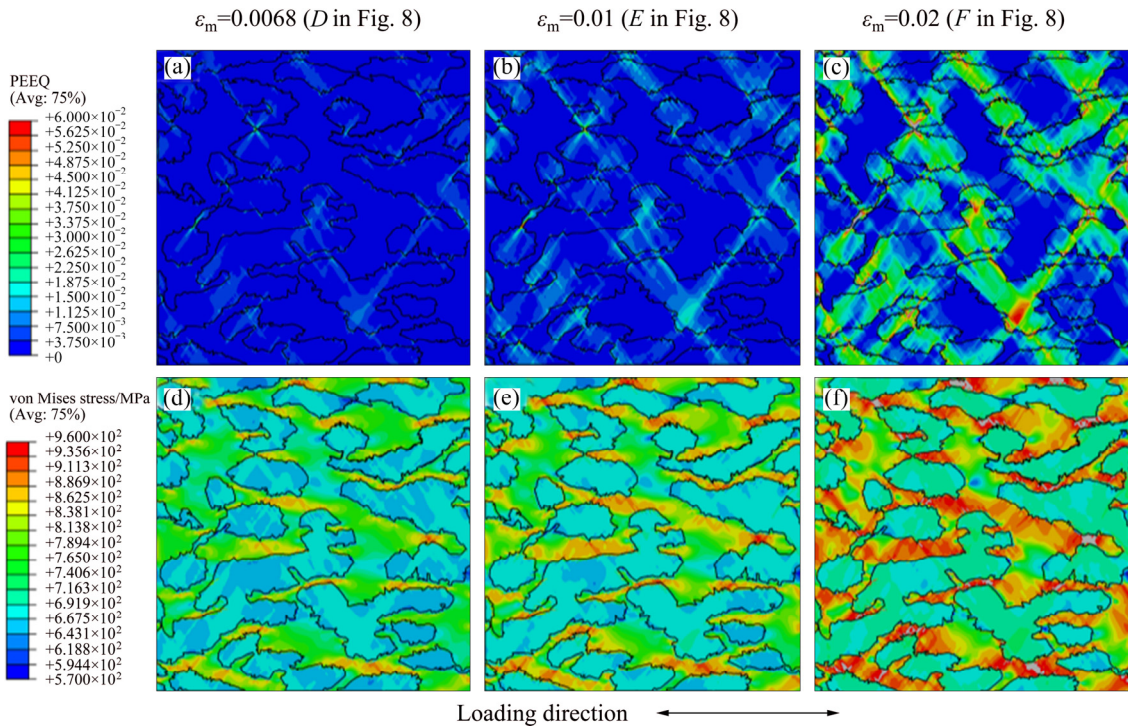


Fig. 10 Distributions of equivalent plastic strain (PEEQ) and von Mises stress at different macroscopic strains (ϵ_m) in HAZ (Grain boundaries are traced by black pen)

phase and stress localization in the harder phase are larger in the HAZ (Figs. 10(c) and (f)). Therefore, the stress and strain distributions in the HAZ are more inhomogeneous.

4.3 Comparison of strain localization behavior between BM and HAZ

To quantify the extent of strain inhomogeneity of different phases in the welded joints, the average

equivalent plastic strain is calculated at different macroscopic strains by the following formula:

$$\varepsilon_{p,i} = \frac{1}{V_i} \int \varepsilon_p dV_i \quad (9)$$

where i refers to the kind of phase, $\varepsilon_{p,i}$ is the average phase plastic strain, and V_i is the volume of phase i . Figure 11 shows that the distribution of the average plastic strain of constituent phases in two zones of the welded joints at different macroscopic strains. It is found the growing rate of the average plastic strain in each phase is almost a constant. In the BM, as the macroscopic strain increases, the average plastic strain of α_p phase increases significantly, in contrast, it increases slightly in β_t phase (blue line). Similar results occur in the HAZ (red line). However, the extent of the strain partitioning in the HAZ is more serious: at the macroscopic strain of 0.1, in the BM, the average plastic strain in α_p phase is 0.07 higher than that in β_t phase; in the HAZ, the average plastic strain in α_p phase is 0.11 higher than that in the α' phase.

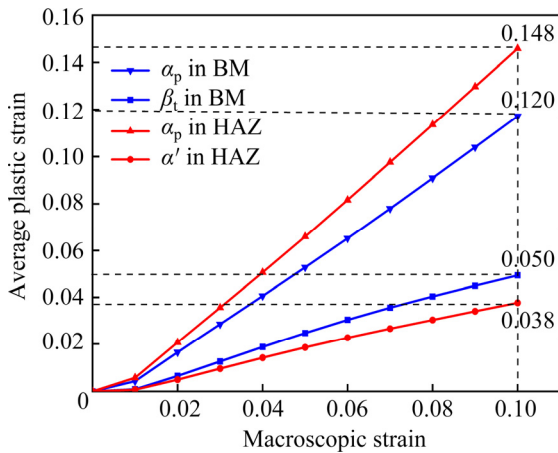


Fig. 11 Average plastic strain of constituent phases at different macroscopic strains

It is believed that the inhomogeneity of microstructure is a crucial factor, which induces the instability of local plastic deformation and results in the appearance of the plastic strain localization in the dual phases [29–31]. To realize the distribution of the strain localization visually, the global view of equivalent plastic strain contours for the α_p phase within the RVEs at the macroscopic strain level of 0.1 is shown in Fig. 12. It is observed that a large number of the strain localization bands (SLBs) are triggered by the plastic strain localization in α_p phase (PEEQ larger than 0.7). The plastic strain

localization zone mainly distributes in two regions according to the simulated results: the intersection of SLBs and the phase boundary, i.e. the places with red circles in Fig. 12. These zones may be the “dangerous zone” where failure usually initiates [22,23]. Besides, the maximum equivalent plastic strain value in the HAZ is 11.46, higher than that in the BM (3.257). A finding could be obtained by comparing Fig. 12(a) with Fig. 12(b), if decreasing the strength discrepancy of both phases, the strain and strain gradients of SLBs would be effectively lower, which is consistent with the results of Ji et al [21].

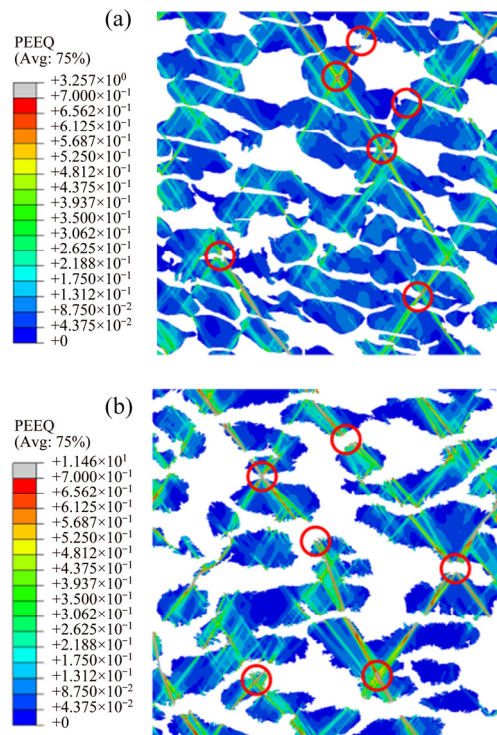


Fig. 12 Equivalent plastic strain distribution of α_p phase at macroscopic strain of 0.1: (a) BM; (b) HAZ

At the macroscopic strain of 0.1, Fig. 13 quantifies the frequency of equivalent plastic strain value for constituent phases of different zones in the welded joints. It is found that most of the plastic strains concentrate in α_p phase, agreeing with the previous discussion. A bell-shaped curve with lower peak value (PEEQ=0.095) and narrower strain range is distributed in α_p phase of the BM, indicating that the relatively small areas in α_p phase bear the majority of deformation. Compared with the BM, the HAZ has higher frequency value (PEEQ>0.2), which may be a larger possibility to induce strain localization in α_p phase.

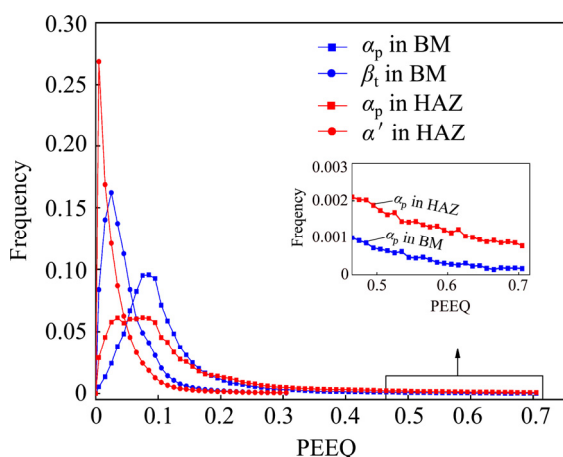


Fig. 13 Frequency distribution of PEEQ at macroscopic strain of 0.1

5 Conclusions

(1) The macroscopic mechanical properties different zones in TA15 electron beam welded joints are determined by the microscope elastic–plastic behavior of their constituent phase. The simulated results of the stress–strain curves based on the realistic microstructure are in good agreement with the tensile test results.

(2) Microstructure inhomogeneity resulted from the mechanical property difference between the two phases gives rise to the inhomogeneous stress–strain distribution during the tensile process. The incompatible deformation between the constituent phases usually localizes along the softer α_p phase where failure initiates in the form of localized plastic strain.

(3) The microstructure inhomogeneity exists in the BM and HAZ of TA15 titanium alloy welded joints. Compared with the BM, the mechanical property difference of constituent phases in the HAZ is larger, leading to more serious strain localization in α_p phase.

References

- [1] XU Wei-feng, ZHANG Zhen-lin. Microstructure and mechanical properties of laser beam welded TC4/TA15 dissimilar joints [J]. Transactions of Nonferrous Metals Society of China, 2016, 26(12): 3135–3146.
- [2] YANG Xia-wei, LI Wen-ya, LI Hong-yu, YAO Shuo-tian, SUN Yi-xuan, SUN Yi-xian, MEI Lu. Microstructures and microhardness for sheets and TIG welded joints of TA15 alloy using friction stir spot processing [J]. Transactions of Nonferrous Metals Society of China, 2018, 28(1): 55–65.
- [3] BANERJEE D, WILLIAMS J C. Perspectives on titanium science and technology [J]. Acta Materialia, 2013, 61(3): 844–879.
- [4] FALL A, MONAJATI H, KHODABANDEH A, FESH-ARAKI M H, CHAMPLAUD H, JAHAZI M. Local mechanical properties, microstructure, and microtexture in friction stir welded Ti–6Al–4V alloy [J]. Materials Science and Engineering A, 2019, 749: 166–175.
- [5] ÇAM G. Friction stir welded structural materials: Beyond Al-alloys [J]. International Materials Reviews, 2011, 56(1): 1–48.
- [6] KASHAEV N, VENTZKE V, ÇAM G. Prospects of laser beam welding and friction stir welding processes for aluminum air frame structural applications [J]. Journal of Manufacturing Processes, 2018, 36: 571–600.
- [7] DOS SANTOS J, ÇAM G, TORSTER F, INFRAN A, RIEKEHR S, VENTZKE V, KOÇAK M. Properties of power beam welded steels, Al- and Ti-alloys: Significance of strength mismatch [J]. Welding in the World, 2000, 44(6): 42–64.
- [8] WANG Gong-qiang, CHEN Zhi-yong, LI Jin-wei, LIU Jian-rong, WANG Qing-jiang, YANG Rui. Microstructure and mechanical properties of electron beam welded titanium alloy Ti-6246 [J]. Journal of Materials Science and Technology, 2018, 34: 570–576.
- [9] XIE Pu, ZHAO Hai-yan, WU Bing, GONG Shui-li. Using finite element and contour method to evaluate residual stress in thick Ti–6Al–4V alloy welded by electron beam welding [J]. Acta Metallurgica Sinica, 2015, 28(7): 922–930.
- [10] CAM G, FLOWER H M, WEST D R F. Solid state phase transformations in Ti–Al–C and Ti–Al–Nb–C alloys [J]. Materials Science and Technology, 1991, 7(7): 587–591.
- [11] CAM G, FLOWER H M, WEST D R F. Constitution of Ti–Al–C alloys in the temperature range 1250–750 °C [J]. Materials Science and Technology, 1991, 7(6): 505–511.
- [12] SUN Q J, XIE X. Microstructure and mechanical properties of TA15 alloy after thermo-mechanical processing [J]. Materials Science and Engineering A, 2018, 724: 493–501.
- [13] SUN X, CHOI K S, LIU W N, KHALEEL M A. Predicting failure modes and ductility of dual phase steels using plastic strain localization [J]. International Journal of Plasticity, 2009, 25(10): 1888–1909.
- [14] GHASSEMI-ARMAKI H, CHEN P, BHAT S, SADAGOPAN S, KUMAR S, BOWER A. Microscale-calibrated modeling of the deformation response of low-carbon martensite [J]. Acta Materialia, 2013, 61: 3640–3652.
- [15] DAO M, CHOLLA COOP N, VLIET K J V, VENKATESH T A, SURESH S. Computational modeling of the forward and reverse problems in instrumented sharp indentation [J]. Acta Materialia, 2001, 49(19): 3899–3918.
- [16] MUKHOPADHYAY N K, PAUFLER P. Micro- and nano-indentation techniques for mechanical characterisation of materials [J]. International Materials Reviews, 2006, 51(4): 209–245.
- [17] SEOK M Y, KIM Y J, CHOI I C, ZHAO Y K, JANG J I. Predicting flow curves of two-phase steels from spherical nanoindentation data of constituent phases: Isostrain method vs. non-isostrain method [J]. International Journal of Plasticity, 2014, 59: 108–118.

- [18] LEE J, LEE C, KIM B. Reverse analysis of nano-indentation using different representative strains and residual indentation profiles [J]. *Materials and Design*, 2009, 30(9): 3395–3404.
- [19] SHI R, NIE Z, FAN Q, LI G. Elastic plastic deformation of TC6 titanium alloy analyzed by in-situ synchrotron based X-ray diffraction and microstructure based finite element modeling [J]. *Journal of Alloys and Compounds*, 2016, 688: 787–795.
- [20] MOEINI G, RAMAZANI A, HILDEBRAND J, ROESSLER C, KOENKE C. Study of the effect of microstructural variation on the low cycle fatigue behavior of laser welded DP600 steel: Simulation and experimental validation [J]. *Materials Science and Engineering A*, 2018, 730: 232–243.
- [21] JI Zhe, YANG He, LI Hong-wei. Predicting the effects of microstructural features on strain localization of a two-phase titanium alloy [J]. *Materials and Design*, 2015, 87: 171–180.
- [22] ZHANG Cheng-ze, GONG Bao-ming, DENG Cai-yan, WANG Dong-po. Computational prediction of mechanical properties of a C–Mn weld metal based on the microstructures and micromechanical properties [J]. *Materials Science and Engineering A*, 2017, 685: 310–316.
- [23] ZHANG Cheng-ze, GONG Bao-ming, DENG Cai-yan, WANG Dong-po. Orientation dependence of deformation and failure in a C–Mn weld metal [J]. *Journal of Materials Processing Technology*, 2017, 250: 363–371.
- [24] NIX W D, GAO H J. Indentation size effects in crystalline materials: A law for strain gradient plasticity [J]. *Journal of the Mechanics and Physics of Solids*, 1998, 46(3): 411–425.
- [25] RODRIGUEZ R, GUTIERREZ I. Correlation between nanoindentation and tensile properties: Influence of the indentation size effect [J]. *Materials Science and Engineering A*, 2003, 361(1–2): 377–384.
- [26] OLIVER W C, PHARR G M. Measurement of hardness and elastic modulus by instrumented indentation: Advances in understanding and refinements to methodology [J]. *Journal of Materials Research*, 2004, 19(1): 3–20.
- [27] CHOI K S, LIU W N, SUN X, KHALEEL M A. Influence of martensite mechanical properties on failure mode and ductility of dual-phase steels [J]. *Metallurgical and Materials Transactions A*, 2009, 40(4): 796–809.
- [28] TAYLOR M D, CHOI K S, SUN X, MATLOCK D K, PACKARD C E, XU L, BARLAT F. Correlations between nanoindentation hardness and macroscopic mechanical properties in DP980 steels [J]. *Materials Science and Engineering A*, 2014, 597: 431–439.
- [29] CHOI K S, LIU W N, SUN X, KHALEEL M A. Microstructure-based constitutive modeling of TRIP steel: Prediction of ductility and failure modes under different loading conditions [J]. *Acta Materialia*, 2009, 57(8): 2592–2604.
- [30] HAN Q H, KANG Y L, HODGSON P D, STANFORD N. Quantitative measurement of strain partitioning and slip systems in a dual-phase steel [J]. *Scripta Materialia*, 2013, 69(1): 13–16.
- [31] MARVI-MASHHADI M, MAZINANI M, REZAEI-BAZZAZ A. FEM modeling of the flow curves and failure modes of dual phase steels with different martensite volume fractions using actual microstructure as the representative volume [J]. *Computational Materials Science*, 2012, 65: 197–202.

组织不均匀性对 TA15 电子束焊焊接接头 不同区域力学性能的影响

邓彩艳¹, 刘策¹, 龚宝明¹, 张承泽², 刘畅¹, 刘永¹

1. 天津大学 材料科学与工程学院 天津市现代连接技术重点实验室, 天津 300350;

2. 长光卫星技术有限公司, 长春 130000

摘要: 基于微观力学有限元分析方法, 研究 TA15 电子束焊焊接接头不同区域组织不均匀性对力学性能的影响。基于压痕尺寸效应, 通过纳米压痕试验确定母材和热影响区组成相的力学性能。结果表明, 母材和热影响区的模拟拉伸结果和宏观拉伸试验结果具有良好的一致性。组成相变形的不协调倾向于沿着初生 α 相集中, 失效通常以应变集中的形式萌生。相较于母材, 热影响区组成相的力学性能差异较大, 应变集中更为严重。

关键词: 组织不均匀性; 应变集中; 电子束焊接; 钛合金; 有限元分析

(Edited by Wei-ping CHEN)